

Solar wind stream interaction regions without sector boundaries

M. Neugebauer

Lunar and Planetary Laboratory, University of Arizona, Tucson, Arizona, USA

P. C. Liewer, B. E. Goldstein, and X. Zhou

Jet Propulsion Laboratory, California Institute of Technology, Pasadena, California, USA

J. T. Steinberg

Los Alamos National Laboratory, Los Alamos, New Mexico, USA

Received 1 March 2004; revised 14 May 2004; accepted 28 June 2004; published 9 October 2004.

[1] During periods of high solar activity when there are many sources of solar wind on the solar disk, a spacecraft occasionally encounters consecutive solar wind streams with the same magnetic polarity. The low-speed wind in the region of interaction between the two streams exhibits many of the same features as, but has some differences from, the low-speed wind that includes crossings of the heliospheric current sheet (HCS) where the direction of the heliospheric magnetic field reverses. The non-HCS slow wind exhibits many of the same small-scale structures usually associated with the slow wind around the HCS; these include discontinuous stream interfaces and other discontinuities, magnetic holes, and low-entropy structures. These entropy holes do not appear to have the same origin as the plasma sheets observed near the HCS, however. The helium abundances and heavy ion charge states in the non-HCS regions are not significantly different from those in HCS-associated regions. Some of the dynamical properties of the non-HCS regions differ from those found near the HCS; the regions between leading and trailing stream interfaces have a shorter duration or scale size, greater minimum speed, and lower peak and average densities. No correlation could be found between the non-HCS slow wind and visible coronal streamers.

INDEX TERMS: 2164 Interplanetary Physics: Solar wind plasma; 2169 Interplanetary Physics: Sources of the solar wind; 2134 Interplanetary Physics: Interplanetary magnetic fields; 7511 Solar Physics, Astrophysics, and Astronomy: Coronal holes; **KEYWORDS:** interaction regions, solar wind

Citation: Neugebauer, M., P. C. Liewer, B. E. Goldstein, X. Zhou, and J. T. Steinberg (2004), Solar wind stream interaction regions without sector boundaries, *J. Geophys. Res.*, 109, A10102, doi:10.1029/2004JA010456.

1. Introduction

[2] The structure of the solar wind at solar minimum is sometimes very simple, with high-speed streams emanating from polar coronal holes and a heliospheric current sheet (HCS) circling the Sun at lower latitudes to separate the magnetic topology into two magnetic sectors. When the Sun is active, the structure of the solar wind is much more complex. At activity maximum the wind and field typically originate in about a dozen disjoint regions [Schrijver and Derosa, 2003]. At solar activity maximum the quasi-stationary solar wind comes both from coronal holes (as defined by observations at the He 1083 nm wavelength) at intermediate latitudes and from open field lines in active regions [Levine, 1977; Neugebauer *et al.*, 2002; Schrijver and Derosa, 2003; Liewer *et al.*, 2003]. The structure of the solar wind is further complicated by transient coronal mass ejections whose origins tend to cluster around the HCS.

[3] It is therefore not surprising that when the Sun is active and accelerates solar wind from many sources, a

heliospheric spacecraft should occasionally encounter consecutive solar wind streams from neighboring sources with the same magnetic polarity. The slow wind in the interaction region between those two streams would have no HCS. Two such cases were pointed out in a study of solar wind sources at solar maximum by Neugebauer *et al.* [2002]. In the present paper we examine the properties of a set of seven quasi-stationary non-HCS interaction regions observed with the Ulysses and ACE spacecraft and compare those properties to what is observed in typical HCS interaction regions.

[4] To set the stage, we remind the reader that the inter-stream or interaction regions between two high-speed streams separated by the HCS typically exhibit lower speed, lower temperature, higher density, more variable and usually lower helium abundance, and higher ionization states of heavy ions than is seen in the cores of the streams themselves. On average, the extrema are centered at or near the HCS [Borrini *et al.*, 1981]. In many cases the shift between fast and slow wind occurs discontinuously at structures called stream interfaces [Gosling *et al.*, 1978], but often the changes across the interface are more gradual. At the stream interface on the leading edge of the second or

following stream, there is also a typical swing of the azimuthal flow direction first from east of the Sun and then from west of the Sun. Additionally, the flow between streams with opposite polarities exhibits abundant other discontinuities: These include many tangential discontinuities with large jumps in density, temperature, composition, and field strength; sometimes multiple crossings of the HCS; and relatively rare slow shocks created by the stream interactions. It has been suggested that the slow solar wind originates at the boundaries of the sources of the fast wind where the expansion rate is greatest [Wang and Sheeley, 1990] and where reconnection between open and closed field lines releases fresh plasma [Schwadron *et al.*, 1999]. Alternatively, Habbal *et al.* [2001] suggest that the quiet corona between coronal holes is a source of slow solar wind. No matter what the source, these slow, dense interstream flows are believed to be the interplanetary counterparts of coronal streamers seen on the limb of the Sun [e.g., Feldman *et al.*, 1981; Gosling *et al.*, 1981; Bavassano *et al.*, 1997].

2. Identification of Events

[5] The analysis was based on solar wind data acquired by the Ulysses and ACE spacecraft. For Ulysses, ion and electron spectra were obtained by the Solar Wind Observations Over the Poles of the Sun instrument [Bame *et al.*, 1992], while the magnetic field was measured by a vector helium magnetometer [Balogh *et al.*, 1992]. For ACE, ion and electron data were from the Solar Wind Electron, Proton, and Alpha Monitor [McComas *et al.*, 1998], and the magnetic field data were from the instrument MAG [Smith *et al.*, 1998].

[6] The search for candidate events was based on hourly averaged plots of solar wind speed color coded according to the polarity of the heliospheric magnetic field. For ACE the polarity was called positive if the longitude of the magnetic field direction was between 45° and 225° , and it was negative for longitudes outside that range. Figure 1 is an example of such a plot. It shows ACE data taken on days 43–70, 1999, with negative (inward) polarity plotted in blue and positive polarity plotted in red. The set of plots was examined for the occurrence of consecutive high-speed streams with the same polarity. Examples in Figure 1 include days 43–52 and days 60–68. A candidate was eliminated from further consideration if the presence of plasma from a coronal mass ejection (CME) was suggested by the presence of an unusually low proton temperature relative to the observed speed, a high helium abundance, a magnetic cloud, or a high ionization state of Fe ions as determined by the Solar Wind Ion Composition Spectrometer (SWICS) instruments on Ulysses and ACE [Gloeckler *et al.*, 1992, 1998]. Slow streams interrupted by CME-associated fast streams, such as those in Figure 1 with velocity peaks on days 49 and 66, were eliminated for that reason.

[7] Similar analyses were carried out for Ulysses. The only difference was that the relation between the field direction and polarity was more complex because of the dependence of the spiral angle on solar distance and latitude. For Ulysses, polarity P was defined as the cosine of the angle between the measured field direction in the RT

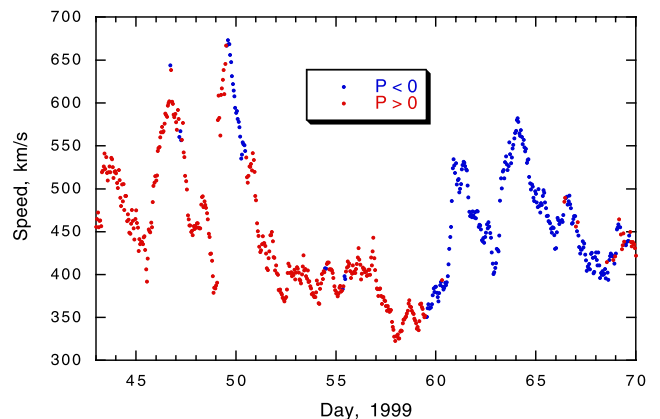


Figure 1. Hourly averages of speed measured by ACE during Carrington rotation 1946. The data are color coded according to the polarity of the heliospheric magnetic field, with red (blue) denoting outward (inward) fields.

plane and the expected direction of an outwardly oriented Parker spiral. Specifically,

$$P = (B_R - \Omega R \cos \lambda B_T / V) / \left\{ \sqrt{[1 + (\Omega R \cos \lambda / V)^2]} \sqrt{(B_R^2 + B_T^2)} \right\}, \quad (1)$$

where B_R and B_T are the radial and tangential components of the field, respectively, V is solar wind speed, R is solar distance, Ω is the solar rotation rate, and λ is heliographic latitude. A latitude-independent value of $\Omega = 2.7 \times 10^{-6} \text{ s}^{-1}$ (corresponding to a sidereal rotation period of 25.4 days) was used. The field was deemed to be outward for $P = 0$ to $+1$ and inward for $P = -1$ to 0 .

[8] The next test of candidate events detected by either spacecraft was the determination of the probable solar source of each of the fast streams. That was done by the mapping process described by Neugebauer *et al.* [2002]. Briefly, a two-step process was used. In step 1 the wind was mapped from the spacecraft back to a source surface at 2.5 solar radii on the assumption of constant, radial flow at the speed measured by the spacecraft. In step 2 a potential field source surface model was used together with the synoptic photospheric magnetic field measured at Kitt Peak National Observatory (KPNO) to trace the magnetic field and solar wind streamlines from the source surface to the photosphere. Estimates of the accuracy of this mapping process have been discussed by Neugebauer *et al.* [1998]. An interaction region was used in the study only if each fast stream mapped to a separate source with magnetic polarity matching that observed at the spacecraft. Consecutive fast streams were not retained if they both mapped to the same polar coronal hole.

[9] Figure 2 (bottom) illustrates the source identifications for Carrington rotation (CR) 1946, corresponding to the field and polarity data shown in Figure 1. The boundaries and polarities of the He 1083 nm coronal holes reported by KPNO are shown in black. The KPNO magnetogram data are shown as red and blue background splotches which indicate the field strength, where red (blue) denotes outward (inward) fields. The tails of the arrows running across

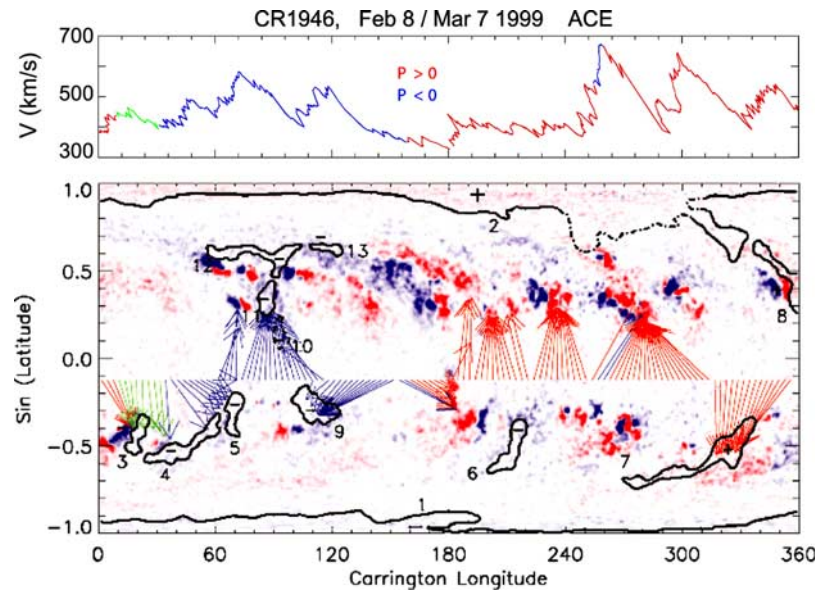


Figure 2. (top) Same data as in Figure 1 plotted as a function of longitude on the source surface. (bottom) Magnetogram, coronal hole data, and mapped source locations for ACE for Carrington rotation (CR) 1946. Photospheric magnetic field strength and polarity as measured by Kitt Peak National Observatory (background red and blue features) are shown. Boundaries of coronal holes determined by observations in He 1083 nm (black lines) are shown. The field polarity is indicated by red (outward fields) or blue (inward) in the magnetograph data and by plus (outward) or minus (inward) signs for the coronal holes. The tails of the arrows mark the source surface foot points of the solar wind observed by ACE, while the arrow heads indicate the photospheric locations of the field lines threading each of the foot points. The arrows are colored according to the observed polarity of the heliospheric magnetic field: red (outward), blue (inward), and green (mixed polarity).

Figure 2 show the trace of the ACE data mapped back to the source surface, whereas the heads of the arrows denote the computed source regions. Red (blue) arrows indicate that ACE detected positive (negative) polarities at that time. Green arrows denote mixed polarity. Figure 2 (top) is a plot of the same data as in Figure 1 but now presented as a function of longitude on the source surface. The sources corresponding to the fast streams in Figure 1 before and after day 45 are seen in Figure 2 on either side of longitude 315° . Before day 45 (at longitudes $>315^\circ$) the wind mapped to a large positive coronal hole at southern midlatitudes. After day 45 (longitudes $<315^\circ$) the source appeared to be the leading, positive polarity part of a bipolar active region. The division between the streams observed before and after day 63 can be seen at $\sim 115^\circ$ longitude, where the source jumped between southern and northern midlatitude coronal holes, both with negative polarity.

[10] Table 1 lists the seven same-polarity interaction regions, called “events,” included in this study. Table 1 also gives the dates of observation of the minimum speed between the streams and the spacecraft locations at those times. For Ulysses the location is given in terms of solar distance and heliographic latitude. ACE was always situated in a halo orbit around the L1 LaGrange point sunward of Earth. The fifth column gives the Carrington rotation number of the synoptic field data used in the mapping. The last column gives, in temporal order, the types of the two sources. The coronal hole designation is used only for those features reported by KPNO on the basis of He 1083 nm observations. Active regions were identified as regions

of high magnetic field strength. The events shown around days 45 and 63 in Figures 1 and 2 are included as events 4 and 5. Some features of event 6 have been discussed previously by Neugebauer *et al.* [2002].

[11] Each of the events listed in Table 1 was studied using high-resolution plasma data. Sections 3, 4, and 5 present those data for events 5, 6, and 7, respectively. The detailed discussion of those three events is followed by sections 6, 7, and 8 based on all seven events.

3. Event 5: ACE Observations on Days 61–63, 1999

[12] Figure 3 shows the high-resolution plasma and field data for event 5. Only the low-speed region between days 62.0 and 63.5 is included. Figure 3a shows solar wind speed

Table 1. Times and Places of Non-HCS Interstream Events Included in the Study^a

Event	Spacecraft	Year/Day	Location	CR	Sources
1	Ulysses	1995/066	1.34 AU, 2°N	1893	LLCH to PCH
2	Ulysses	1995/083	1.35 AU, 16°N	1893	LLCH to PCH
3	Ulysses	1998/107	5.4 AU, 6°S	1934	AR to ARCH
4	ACE	1999/044	L1	1946	LLCH to AR
5	ACE	1999/062	L1	1946	LLCH to LLCH
6	ACE	1999/252	L1	1953	ARCH to LLCH
7	Ulysses	2001/150	1.34 AU, 11°N	1976	AR to ARCH

^aAR, active region; ARCH, active region adjacent to a coronal hole; LLCH, low-latitude coronal hole; PCH, polar coronal hole; and CR, Carrington rotation.

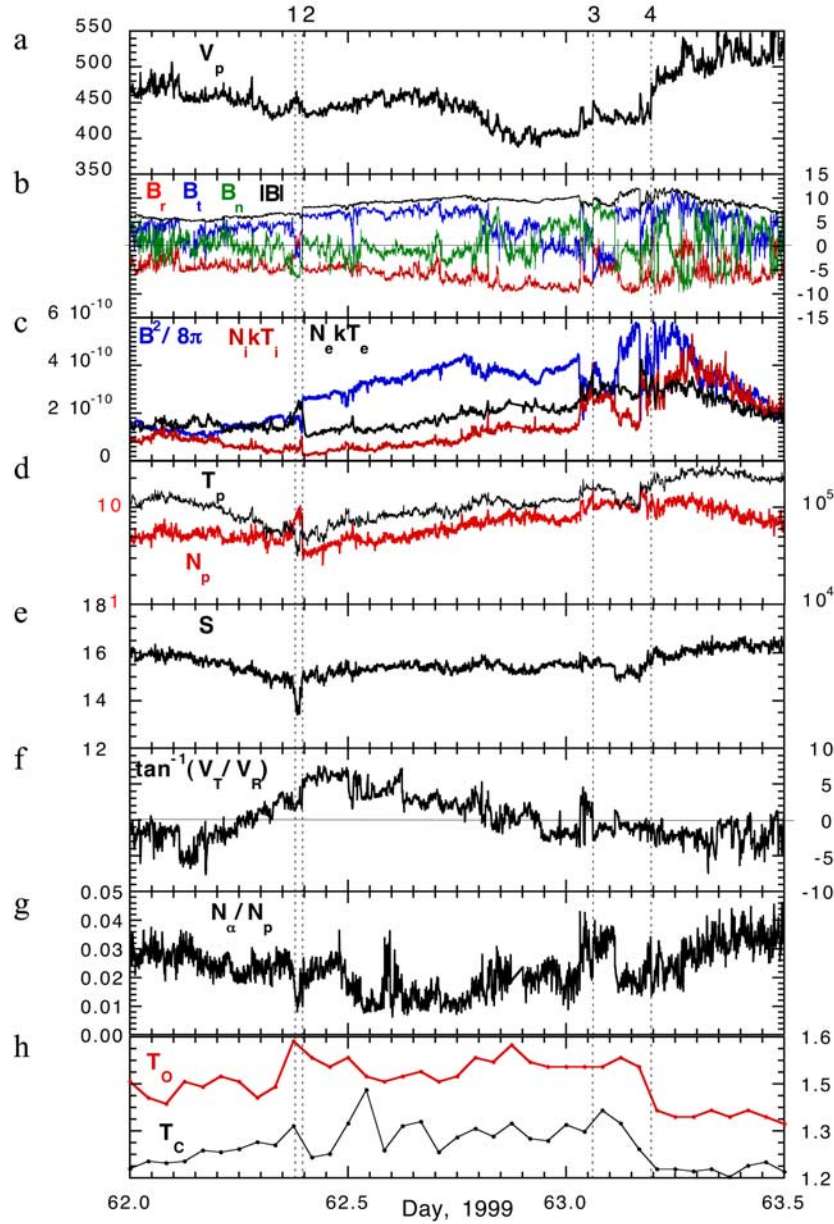


Figure 3. Observed plasma parameters for event 5: (a) proton speed; (b) RTN coordinates and magnitude of the magnetic field; (c) magnetic, ion, and electron pressures; (d) proton density and temperature; (e) entropy per proton; (f) azimuthal flow angle; (g) helium abundance; and (h) ionization temperatures calculated from the charge state ratios of oxygen and carbon. The dashed vertical lines denote specific discontinuities. See the text for greater detail.

in km s^{-1} at a resolution of 64 s, which reached a minimum late on day 62. Figure 3b shows the RTN components and the magnitude of the magnetic field in units of nT at a resolution of 16 s. The pressures (in dyn cm^{-2}) contributed by the magnetic field and the ion and electron thermal pressures are shown in Figure 3c; the ion pressure is the sum of the proton and alpha particle pressures. Figure 3d shows the proton density N_p (in cm^{-3}) and temperature T_p (in K) on logarithmic scales. Those data are combined to form the entropy per proton, defined as $S = \ln(T_p^{3/2}/N_p)$, displayed in Figure 3e. Next, in Figure 3f is the azimuth angle of the solar wind flow vector, in degrees, $\varphi = \tan^{-1}(V_T/V_R)$; φ is positive for flow from the east of the

Sun. In Figure 3g the helium abundance is expressed as the ratio of the alpha particle to proton densities, N_α/N_p . Finally, in Figure 3h, coronal freezing-in ionization temperatures, in units of 10^6 K, are calculated from the ratios of $\text{O}^{7+}/\text{O}^{6+}$ and $\text{C}^{5+}/\text{C}^{6+}$ on the basis of the model of *Arnaud and Rothenflug* [1985]. These heavy ion data were acquired by the SWICS instrument on ACE [*Gloeckler et al.*, 1998]; the time resolution is 1 hour. The vertical dashed lines, labeled 1–4 and hereinafter referred to as D1–D4, denote only a few of the many discontinuities in the plasma and field properties.

[13] Perhaps the most notable feature in Figure 3 is the sharp dip in proton entropy associated with a density increase and temperature decrease between discontinuities

D1 and D2 near day 62.4. We call this feature an “entropy hole.” Figure 3f shows that this feature coincided with a major turning point in the east-west flow pattern. Figure 3b shows that inside the entropy hole the field direction was nearly southward, which was very different from the approximate Parker spiral field outside it. The data in Figure 3c indicate that the total pressure (ion plus electron plus field) went from 3.1×10^{-10} dyn cm $^{-2}$ before the hole to 4.5×10^{-10} dyn cm $^{-2}$ within it to 4.1×10^{-10} dyn cm $^{-2}$ behind it. Although those data indicate that the entropy hole may have been expanding and accelerating, the approximate $\pm 25\%$ uncertainty in the temperature of each species suggests that the possibility of pressure balance is not ruled out. Principal axis analyses of discontinuities D1 and D2 showed that D1 was probably a rotational discontinuity, while D2 was a tangential discontinuity with a normal direction of (0.792, 0.602, -0.095) in RTN coordinates. This normal direction can be combined with the 24 min of elapsed time between D1 and D2 and the 450 km s^{-1} solar wind speed to calculate a spatial thickness of 8×10^5 km. Another broader, less deep entropy hole can be seen between days 63.1 and 63.2.

[14] The small discontinuity identified as D3 meets all the criteria of a reverse slow shock. The coplanarity theorem was used to determine the shock normal and the field bent toward that normal direction as the shock passed the spacecraft. The normal component of the flow in the shock frame was less than $V_A \cos \theta_{Bn}$ (where V_A is the Alfvén speed and θ_{Bn} is the angle between the field and the shock normal) both upstream and downstream and was greater (less) than the slow wave speed upstream (downstream) of the discontinuity.

[15] The discontinuity D4 fits all the criteria for leading edge discontinuous stream interfaces discussed in section 1. The location of the trailing stream interface near day 62.4 is problematic. The composition and ionization temperature data in Figures 3g and 3h suggest that D1 may be a stream interface, but the principal axis analysis showed a large normal component of the magnetic field across that discontinuity.

[16] Another noteworthy feature in Figure 3 is the very low helium abundance, with the ratio N_α/N_p dipping slightly below 0.01. The helium abundance was low not only in the entropy dip between D1 and D2 but at other times as well. Finally, we note that the ionization temperature was higher in the low-speed region between D1 and D4 than in the surrounding high-speed streams.

4. Event 6: ACE Observations on Day 252, 1999

[17] This event occurred during CR 1953, which was studied in detail by Neugebauer *et al.* [2002]. Figure 2 of that paper mapped the source regions for both ACE and Ulysses in a format similar to that of Figure 2 of this paper. The transition associated with this event occurred near Carrington longitude 125° and corresponded to a change of source from the inward polarity fields outside a negative polarity coronal hole at $\sim 30^\circ\text{N}$ to another negative polarity coronal hole at lower latitude. The high-resolution data are shown in Figure 4 in the same format as Figure 3.

[18] We interpret discontinuities D1 and D6 as the stream interfaces associated with the trailing edge of the first

stream and the leading edge of the second stream, respectively, because of the correlated changes in speed, temperature, density, entropy, flow direction, composition, and ionization temperature.

[19] This event had two entropy holes. The one between D2 and D3 was shown as Figure 13 of Neugebauer *et al.* [2002]. The second one was bounded by D5 and D6, where, as discussed above, D6 might have been the stream interface of the following stream. Neither entropy hole had as great an effect on the flow direction as did the hole in event 5. Within the accuracy of the temperature measurements both entropy holes were in pressure balance with their surroundings.

[20] This event also had a major magnetic hole between D2 and D4 which included but extended beyond the first entropy hole. The discontinuity at the trailing edge of the magnetic hole might have been a reverse slow shock, but we were not able to prove that conjecture because of the very small angular change of the field across the discontinuity and because the relatively low resolution of the plasma data prevented good separation of D4 from a preceding rotational discontinuity. There was an additional, very brief magnetic hole with a large change in field direction near day 252.7.

[21] As in event 5, the helium abundance ratio dipped to 0.01 on several occasions, and the ionization temperatures of oxygen and carbon were greater between the stream interfaces than outside them.

5. Event 7: Ulysses Observations on Day 150, 2001

[22] Figure 5 displays several plasma and field parameters obtained by Ulysses on day 150, 2001 in the same format as Figures 3 and 4. In Figure 5 the time resolutions are 4 min for ions, 17.3 min for electrons, 1 min for the magnetic field, and 3 hours for the heavy ion ionization temperatures. The proton and alpha data have been corrected to remove the instrumental smear by the method described in the appendix of Neugebauer *et al.* [2001]. As before, vertical lines mark the passage of discontinuous changes in the plasma and field properties, referred to as D1–D6.

[23] We identify the discontinuities D1 and D6, with their sudden changes in speed, density, temperature, entropy, and (for D6) flow direction, as clear examples of discontinuous stream interfaces. The pressures shown in Figure 5 were consistent with pressure balance across D1; the total pressure change is difficult to determine because of the variable timings of the several detectors, but there was no obvious imbalance. While there were substantial changes in the ion temperature and anisotropy (not shown) across D1, the magnetic field changed very little. The change in the field was so small that principal axis (minimum variance) analysis (PAA) could not be used to determine the normal to the discontinuity surface. Note, however, that the field was essentially radial until D3. The nature of D6 is not clear because PAA across the principal rise in field magnitude yields a substantial normal component of the field. The field for 2 min preceding the main increase was very noisy, however, with a series of discontinuities. D6 might have been a tangential discontinuity

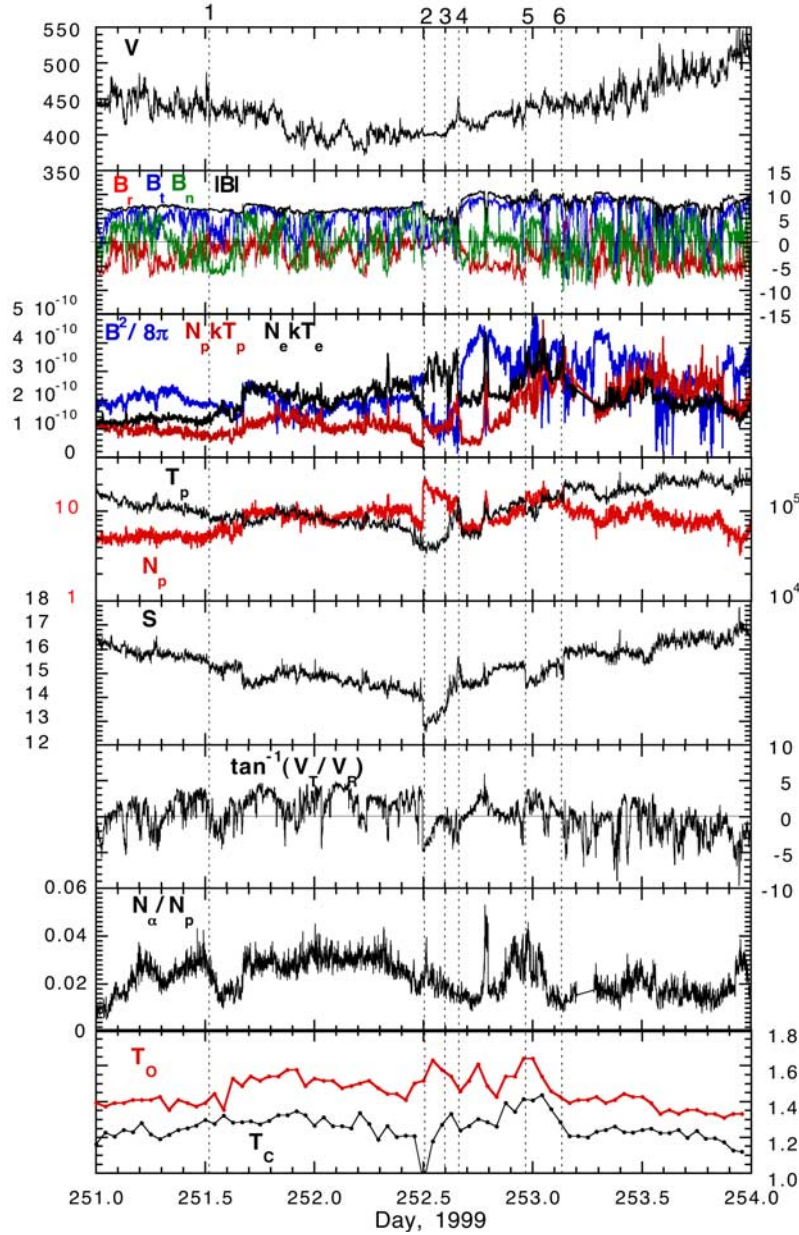


Figure 4. Observed plasma parameters for event 6 in the same format as Figure 3.

across which the field strength, speed, and temperature increased while the density decreased. The high-density, low-temperature, low-entropy plasma extended all the way from D1 to D6, an interval of 13.7 hours, with no conspicuous entropy holes.

[24] The discontinuities D2 and D3 formed the leading edge of a magnetic hole. Principal axis analysis indicates that D2 was a tangential discontinuity, while the nature of D3 is less certain. The magnetic field strength recovered abruptly at D4. Although the eigenvalue ratios returned by PAA do not allow clear identifications of the normal to D4, the change in magnitude across D4 was so large that the discontinuity was most probably tangential.

[25] There was a pressure increase across D5, which could have been a weak forward fast shock. None of the discontinuities marked in Figure 5 could be identified as a slow shock.

[26] The helium abundance was unusually low between D4 and D5, with N_α/N_p dropping as low as 0.005 and averaging 0.010 over that interval. Although the temporal resolution of the heavy ion data was very coarse, those data are consistent with an increase in the ionization temperature between the two stream interfaces.

6. Summary of All Seven Events

[27] Table 2 summarizes the major structures found in each of the seven interstream events included in this study:

[28] Discontinuous stream interfaces could be found in five of the seven events.

[29] All but one of the interstream regions contained one or more distinct entropy holes with the parameter S dropping sharply by an amount ΔS ranging from 0.5 to 2.2. Five of the 12 entropy holes were associated with major changes

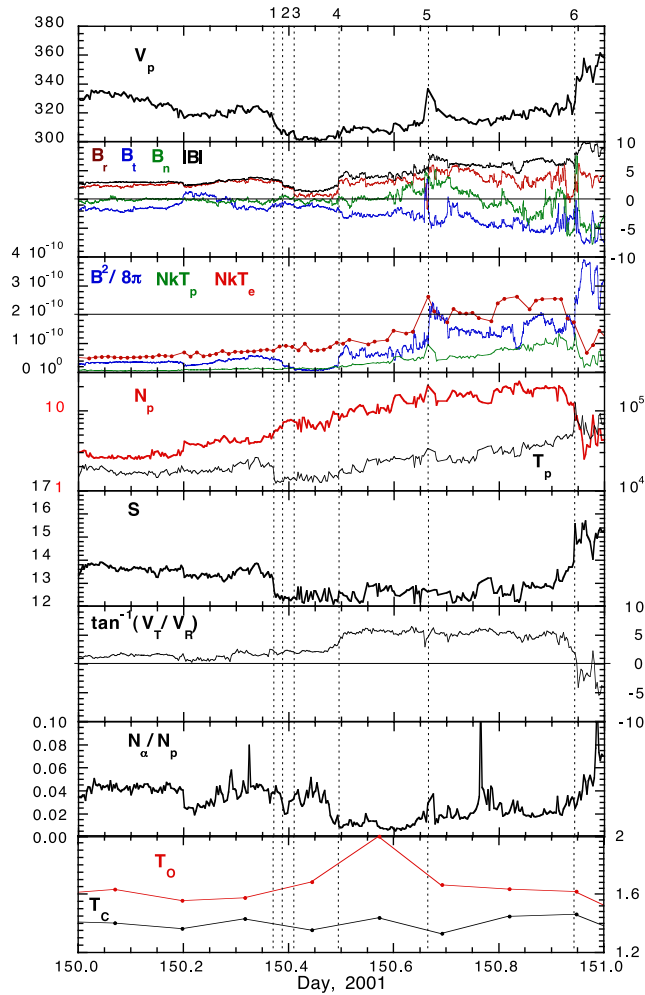


Figure 5. Observed plasma parameters for event 7 in the same format as Figure 3.

in the direction of the magnetic field. There was a brief reversal of the field polarity (as defined by the pitch angle of suprathermal electrons) in the center of the entropy hole in event 3. Event 2 also had a region of reversed polarity for a period of ~ 3 hours, but that reversal was not associated with an entropy hole.

[30] Magnetic holes were detected in five of the seven interstream regions in this study.

[31] Two of the events observed by Ulysses, one at a solar distance of 1.34 AU and the other at 5.4 AU, had fast

Table 2. Structures Seen in Each of the Seven Non-HCS Intervals Studied

Event	Entropy Hole(s)	Stream Interface(s)?	Reverse Polarity Intervals?	Magnetic Hole(s)?	Shocks ^a
1	2 (?)	no	no	no	FFS
2	3	yes	yes	yes	
3	1	no	yes	yes	FFS
4	2	yes	no	yes	
5	2	yes	no	no	RSS
6	2	yes (2) ^b	no	yes	RSS(?)
7	0	yes (2) ^b	no	yes	FFS

^aFFS, forward fast shock; RSS, reverse slow shock.

^bTwo stream interfaces observed.

forward shocks at the leading edges of the following high-speed streams. The reverse slow shocks in events 5 and 6 and the small fast shock in event 7 were probably the result of local effects within the interaction region.

[32] Table 3a presents data on the helium abundances and ionization temperatures of the seven events. In every event the helium abundance reached a minimum value ≤ 0.01 . The third column of Table 3a shows the average helium abundance in the slow wind between the stream interfaces on the trailing edge of the fast stream and the leading edge of the second stream. Approximate boundaries were selected in the absence of discontinuous stream interfaces.

[33] The last two columns of Table 3a present the average oxygen ionization temperatures between the stream interfaces (the column labeled “Slow”) compared to the ionization temperature before the first and after the second stream interface (“Fast”). The ionization temperatures in the interstream regions were always higher than they were in the bounding high-speed streams.

7. Coronal Streamers?

[34] Because the densities in the interstream regions were consistently higher than in the bounding higher-speed streams, especially in the entropy holes, one might expect to see some coronal brightening associated with our seven events. Large Angle and Spectrometric Coronagraph (LASCO) synoptic data were examined to search for such brightenings. Events 1 and 2 preceded the LASCO era, and there were also no LASCO data for event 4. For event 3, there was a suggestion of slight coronal brightening at the appropriate latitude on the west limb, but nothing was seen on the east limb. The best possibility of a coronal signal is the brightening on the east limb for event 5. Figure 6 shows the east limb data from LASCO C2 at 2.5 solar radii, with the approximate locations of the source coronal holes marked by white-outlined boxes. A wispy streak of brightening can be seen between the two sources, located adjacent to the northern source. This streamer, however, got dimmer and narrower with decreasing longitude (increasing time), probably meaning that the streamer passed the limb before the start of 20 February; it could have been associated with

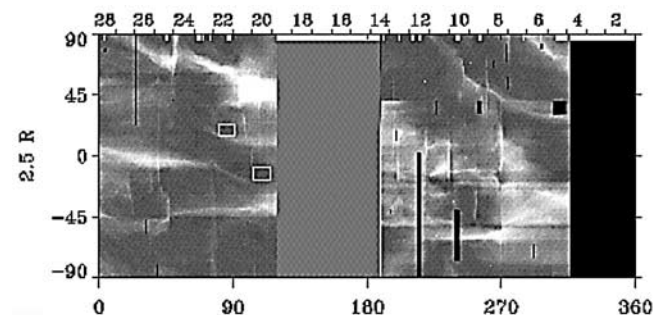


Figure 6. Synoptic coronal data obtained at 2.5 solar radii above the east limb of the Sun by the Large Angle and Spectrometric Coronagraph C2 during Carrington rotation 1946. The lower abscissa is Carrington longitude, and the upper is the date in February 1999. The ordinate is solar latitude. The white-outlined boxes mark the approximate locations of the two coronal holes associated with event 5.

Table 3a. Heavy Ion Properties of Each of the Seven Non-HCS Events in the Study

Event	Minimum N_{α}/N_p	Average N_{α}/N_p	Oxygen Ionization Temperatures, MK	
			Fast	Slow
1	0.003	0.016	1.28	1.35
2	0.010	0.022	1.56	1.78
3	~ 0.010	0.024	1.38	1.63
4	≤ 0.002	≤ 0.007	1.48	1.77
5	~ 0.010	0.019	1.42	1.52
6	~ 0.010	0.026	1.38	1.51
7	0.006	0.022	1.50	1.72
Average	$\leq 0.007 \pm 0.004$	$\leq 0.019 \pm 0.006$	1.43 ± 0.09	1.61 ± 0.16
Oxygen Ionization Temperatures, MK				
			Fast	Slow
Average, von Steiger et al. [2000]			0.94	1.70
Average, Gloeckler et al. [2003] ^a			1.64 ± 0.20	1.78 ± 0.19

the heliographic current sheet which had a north-south direction on the source surface at a longitude of $\sim 160^\circ$. There were no LASCO synoptic data for the west limb passage of that region. For event 6 the synoptic C2 data did not show any brightening between the two sources, and no C3 data were available. The LASCO data for event 7 were too noisy to work with.

8. Summary and Discussion

[35] In most respects the slow solar wind between streams with the same polarity matched the expectations based on the properties of the slow wind surrounding the heliospheric current sheet. As expected, the slow plasma was denser, thermally cooler, but ionizationally hotter, and had a lower, more variable helium content than the surrounding faster plasma. It was also quite highly structured with many examples of discontinuities (stream interfaces, rotational and tangential discontinuities, and fast and slow shocks), magnetic holes, and structures we have called entropy holes.

[36] What is the origin of the entropy holes? Our entropy holes are an order of magnitude thicker than the high-beta (as opposed to high-density) plasma sheets associated with the HCS studied by Winterhalter et al. [1994b]. Crooker et al. [2004] suggest that high-density plasma sheets, with a size distribution which overlaps the size range of our entropy holes, are signatures of small coronal transients formed by reconnection at the tips of helmet streamers at the base of the HCS. Such a model cannot explain the entropy holes discussed here because these holes are far removed from the HCS and are not associated with either sector boundaries or large-scale kinks in the field direction. The fact that most of the entropy holes are bounded by tangential discontinuities implies that they originate at the Sun. We suggest that they may come from isolated sources of solar wind that are too small to be found in the type of map illustrated in Figure 2.

[37] We could identify discontinuous stream interfaces in five of the seven events. This frequency of 5/7 is significantly greater than that reported by Gosling et al. [1978], who found sharp boundaries in approximately one third of

the leading edges of high-speed streams observed at 1 AU by IMP 6, 7, and 8 between 1971 and 1974. Gosling et al. did not, however, have the benefit of heavy ion charge state data to aid in the identification of stream interfaces.

[38] Magnetic holes have preferentially been found near stream interfaces [Klein and Burlaga, 1980] and in interaction regions between fast and slow solar wind [Winterhalter et al., 1994a]. Slow shocks are also most likely to be found in interaction regions [Whang et al., 1996]. From the present study we conclude that those correlations must be independent of any association with the HCS.

[39] The compositional data in Table 3a relate to the properties of the sources of the solar wind independent of interplanetary dynamics. The minimum helium abundances in these non-HCS regions are less than the minimum abundances of ~ 0.020 – 0.035 found by Borrini et al. [1981, Figure 6] on the basis of superposed epoch analyses centered on the heliospheric current sheet. The significance of that difference is questionable, however, because the two sets of data were acquired by different instruments and because some details must have been lost in the superposition process. We have therefore looked at six relatively simple, non-CME-associated HCS crossings observed by ACE in 1999 using the same time resolution as for events 4–6. The HCS-associated, slow-wind events were labeled A–F, and the day numbers of the HCS crossing are given in the first column of Table 3b. The minimum helium abundances in the slow wind around those six HCS crossings are given in the second column of Table 3b; they ranged from 0.003 to 0.014 and averaged 0.006, which is consistent with the minimum values in column 2 of Table 3a. Only three of the event A–F helium abundance minima occurred at or adjacent to the current sheet crossings; the other three minima were found elsewhere in the slow wind between the two stream interfaces. Thus it is not surprising that an HCS-centered superposition of many regions would yield an average value at the HCS greater than the individual minima.

[40] The average helium abundances between stream interfaces are given in the third column of Tables 3a and 3b. It was not possible to confidently identify starting stream interfaces for events E and F because of possible CME plasmas preceding the HCS crossings. From the average values of N_{α}/N_p in Tables 3a and 3b we conclude that there is no statistically significant difference in the helium abundances of HCS and non-HCS interstream regions.

Table 3b. Heavy Ion Properties of Each of the Six HCS-Associated Events

Event/Day 1999	Minimum N_{α}/N_p	Average N_{α}/N_p	Oxygen Ionization Temperatures, MK	
			Fast	Slow
A/013	0.014	0.036	1.46	1.79
B/059	0.006	0.021	1.50	1.69
C/167	0.003	0.017	1.63	1.83
D/276	0.003	0.020	1.49	1.76
E/303	0.005	—	—	2.05
F/337	0.007	—	—	1.66
Average	0.006 ± 0.004	0.024 ± 0.009	1.52 ± 0.08	1.79 ± 0.14

Table 4a. Plasma Properties of the Three Non-HCS Interstream Regions Observed by ACE

Event	Min V_i km s ⁻¹	t_{slow} hours	Max N_p cm ⁻³	$\langle N_p \rangle$ cm ⁻³	Min T_p 10 ³ K	$\langle T_p \rangle$ 10 ³ K	Min B nT	$\langle B \rangle$ nT
4	377	25	10	10	21	45	4.0	8.1
5	389	20	11	8	34	128	5.5	9.3
6	372	39	18	10	31	60	2.0	7.4
Average	379 ± 9	28 ± 10	13 ± 4	9 ± 1	29 ± 7	78 ± 44	3.8 ± 1.8	8.3 ± 1.0

[41] The oxygen ionization temperatures in Tables 3a and 3b reveal consistently lower values in the slow wind between the stream interfaces than in the surrounding faster wind for both non-HCS and HCS events. The event-averaged ionization temperatures in the slow wind for both types of regions are consistent with the ionization temperature of 1.70 MK found in the superposed Ulysses HCS crossings compiled by *von Steiger et al.* [2000, Plate 6]. The fast wind in the present study, however, was ionizationally hotter than the fast wind from the polar coronal holes in the von Steiger et al. analysis. That discrepancy arises from the difference between the speed of the fast wind before and after our events and the speed of the wind from the polar coronal holes considered by *von Steiger et al.* [2000]. Using Ulysses data over a complete solar cycle, *Zurbuchen et al.* [2002] have shown that there is a continuum of ionization charge states and solar wind speeds rather than the bimodal distributions seen at solar minimum. Recently, *Gloeckler et al.* [2003] have determined an average relation between solar wind speed and the ionization temperature of oxygen based on 10 years of Ulysses data (December 1990 to December 2000) over the full Ulysses latitude range ($\pm 80^\circ$). They found V (km s⁻¹) = $844/T_O$ (MK) - 88. The bottom row of Table 3a gives the average oxygen ionization temperatures expected for the non-HCS events calculated from the average fast and slow speeds observed for each event. The averages calculated from the Gloeckler et al. relation agree with the observed averages within their standard deviations. It should be noted, however, that the Gloeckler et al. equation gives consistently higher temperatures for every event for reasons we do not fully understand, except perhaps that their sample included some CME plasma with higher than average ionization temperatures.

[42] Our conclusion from both the alpha particle and heavy ion data is that there are no significant differences in the compositions of the slow solar wind from non-HCS and HCS regions.

[43] Tables 4a and 4b present the principal plasma parameters relevant to interplanetary dynamics. Table 4a was limited to only the three ACE intervals in order to use only those data collected at a single distance from the Sun. The third column, t_{slow} , gives the time, in hours, between stream interfaces. From Tables 4a and 4b it can be seen that the non-HCS events had higher minimum speeds, longer durations, lower peak and average densities, and slightly higher kinetic temperatures and field magnitudes than did the average HCS events. The differences in the durations and minimum speeds can probably be understood on the basis of the closer spacing of the same-polarity source regions than of the source regions separated by the HCS. Although the differences in temperature are not really statistically significant, a trend for higher minimum and average temperatures in the non-HCS events would probably follow from the well-established correlation between speed and temperature. In the HCS events, only half of the minimum temperatures coincided with or were adjacent to the HCS, with the other three found elsewhere in the slow wind. The differences in field strength are also not statistically significant, but such a trend would be consistent with field minima often being found at the HCS itself. The minimum field strengths coincided with HCS crossings for four of the HCS events in our sample of six.

[44] The difference in densities between the two types of regions can be attributed to the fact that in every HCS event the peak density coincided with or was adjacent to a crossing of the HCS. The high densities were thus associated with the small-scale heliospheric plasma sheets described by *Winterhalter et al.* [1994b]. Finally, the lack of a credible connection between the non-HCS interaction regions and visible coronal streamers can probably be explained by the relatively lower densities and shorter durations or extents of those regions compared to the HCS-associated streamer belts.

Table 4b. Plasma Properties of Six HCS-Associated Interstream Regions Observed by ACE in 1999

Event	Min V_i km s ⁻¹	t_{slow} hours	Max N_p cm ⁻³	$\langle N_p \rangle$ cm ⁻³	Min T_p 10 ³ K	$\langle T_p \rangle$ 10 ³ K	Min B nT	$\langle B \rangle$ nT
A	326	45	43	12	14	43	3.7	9.0
B	313	66	30	19	20	50	3.4	9.5
C	265	29	28	11	23	46	1.8	4.7
D	370	70	19	10	20	65	2.2	7.0
E	354	—	33	—	17	—	5.1	—
F	366	—	48	—	44	—	3.5	—
Average	332 ± 40	52 ± 19	33 ± 11	13 ± 4	23 ± 11	51 ± 10	3.3 ± 1.2	7.6 ± 2.2

[45] **Acknowledgments.** The NSO/Kitt Peak magnetograph data were produced cooperatively by NSF/NOAO, NASA/GSFC, and NOAA/SEL. The ACE magnetometer data were provided by N. F. Ness and C. W. Smith through the ACE Science Center, and C. W. Smith sent us the higher-resolution data required to study discontinuities. Some of the work was performed at the Jet Propulsion Laboratory of the California Institute of Technology under contract with the National Aeronautics and Space Administration. The work at Los Alamos was performed under the auspices of the U.S. Department of Energy with financial support from the NASA ACE program.

[46] Shadia Rifai Habbal thanks Nathan A. Schwadron and another referee for their assistance in evaluating this paper.

References

- Arnaud, M., and R. Rothenflug (1985), An updated evaluation of recombination and ionization rates, *Astron. Astrophys. Suppl. Ser.*, **60**, 425.
- Balogh, A., T. J. Beek, R. J. Forsyth, P. C. Hedgecock, R. J. Marquedant, E. J. Smith, D. J. Southwood, and B. T. Tsurutani (1992), The magnetic field investigation on the Ulysses mission: Instrumentation and preliminary scientific results, *Astron. Astrophys. Suppl. Ser.*, **92**, 221.
- Bame, S. J., D. J. McComas, B. L. Barraclough, J. L. Phillips, K. J. Sofaly, J. C. Chavez, B. E. Goldstein, and R. K. Sakurai (1992), The Ulysses solar wind plasma experiment, *Astron. Astrophys. Suppl. Ser.*, **92**, 237.
- Bavassano, B., R. Woo, and R. Bruno (1997), Heliospheric plasma sheet and coronal streamers, *Geophys. Res. Lett.*, **24**, 1655.
- Borrini, G., J. T. Gosling, S. J. Bame, W. C. Feldman, and J. M. Wilcox (1981), Solar wind helium and hydrogen structure near the heliospheric current sheet: A signal of coronal streamers at 1 AU, *J. Geophys. Res.*, **86**, 4565.
- Crooker, N. U., C.-L. Huang, S. M. Lamassa, D. E. Larson, S. W. Kahler, and H. E. Spence (2004), Heliospheric plasma sheets, *J. Geophys. Res.*, **109**, A03107, doi:10.1029/2003JA010170.
- Feldman, W. C., J. R. Asbridge, S. J. Bame, E. E. Fenimore, and J. T. Gosling (1981), The solar origins of solar wind interstream flows: Near-equatorial coronal streamers, *J. Geophys. Res.*, **86**, 5408.
- Gloeckler, G. L., et al. (1992), The solar wind ion composition spectrometer, *Astron. Astrophys. Suppl. Ser.*, **92**, 267.
- Gloeckler, G., et al. (1998), Investigation of solar and interstellar matter using solar wind and pickup ion measurements with SWICS and SWIMS on the ACE spacecraft, *Space Sci. Rev.*, **86**, 497.
- Gloeckler, G., T. H. Zurbuchen, and J. Geiss (2003), Implications of the observed anticorrelation between solar wind speed and coronal electron temperature, *J. Geophys. Res.*, **108**(A4), 1158, doi:10.1029/2002JA009286.
- Gosling, J. T., J. R. Asbridge, S. J. Bame, and W. C. Feldman (1978), Solar wind stream interfaces, *J. Geophys. Res.*, **83**, 1401.
- Gosling, J. T., G. Borrini, J. R. Asbridge, S. J. Bame, W. C. Feldman, and R. T. Hansen (1981), Coronal streamers in the solar wind at 1 AU, *J. Geophys. Res.*, **86**, 5438.
- Habbal, S. R., R. Woo, and J. Arnaud (2001), On the predominance of the radial component of the magnetic field in the solar corona, *Astrophys. J.*, **558**, 852.
- Klein, L., and L. F. Burlaga (1980), Interplanetary sector boundaries 1971–1973, *J. Geophys. Res.*, **85**, 2269.
- Levine, R. H. (1977), Large scale solar magnetic fields and coronal holes, in *Coronal Holes and High Speed Wind Streams*, edited by J. B. Zirker, p. 103, Colo. Assoc. Univ. Press, Boulder.
- Liewer, P. C., M. Neugebauer, and T. Zurbuchen (2003), Active-region sources of solar wind near solar maximum, in *CP679, Solar Wind Ten: Proceedings of the Tenth International Solar Wind Conference*, edited by M. Velli, R. Bruno, and F. Malara, p. 51, Am. Inst. Phys., College Park, Md.
- McComas, D. J., et al. (1998), Solar wind electron proton alpha monitor (SWEPAM) for the Advanced Composition Explorer, *Space Sci. Rev.*, **86**, 563.
- Neugebauer, M., et al. (1998), Spatial structure of the solar wind and comparisons with solar data and models, *J. Geophys. Res.*, **103**, 14,587.
- Neugebauer, M., B. E. Goldstein, D. Winterhalter, E. J. Smith, R. J. MacDowall, and S. P. Gary (2001), Ion distributions in large magnetic holes in the fast solar wind, *J. Geophys. Res.*, **106**, 5635.
- Neugebauer, M., P. C. Liewer, E. J. Smith, R. M. Skoug, and T. H. Zurbuchen (2002), Sources of the solar wind at solar activity maximum, *J. Geophys. Res.*, **107**(A12), 1488, doi:10.1029/2001JA000306.
- Schrijver, C. J., and M. L. Derosa (2003), Photospheric and heliospheric magnetic fields, *Sol. Phys.*, **212**, 165.
- Schwadron, N. A., L. A. Fisk, and T. H. Zurbuchen (1999), Elemental fractionation in the slow solar wind, *Astrophys. J.*, **521**, 859.
- Smith, C. W., et al. (1998), The ACE magnetic fields experiment, *Space Sci. Rev.*, **86**, 613.
- von Steiger, R., N. A. Schwadron, L. A. Fisk, J. Geiss, G. Gloeckler, S. Hefti, B. Wilken, R. F. Wimmer-Schweingruber, and T. H. Zurbuchen (2000), Composition of quasi-stationary solar wind flows from Ulysses/Solar Wind Ion Composition Spectrometer, *J. Geophys. Res.*, **105**, 27,217.
- Wang, Y.-M., and N. R. Sheeley Jr. (1990), Solar wind speed and coronal flux-tube expansion, *Astrophys. J.*, **355**, 726.
- Whang, Y. C., J. Zhou, R. P. Lepping, and K. W. Ogilvie (1996), Interplanetary slow shock observed from Wind, *Geophys. Res. Lett.*, **23**, 1239.
- Winterhalter, D., M. Neugebauer, B. E. Goldstein, E. J. Smith, B. T. Tsurutani, S. J. Bame, and A. Balogh (1994a), Magnetic holes in the solar wind and their relation to mirror-mode structures, *Space Sci. Rev.*, **72**, 201.
- Winterhalter, D., E. J. Smith, M. E. Burton, N. Murphy, and D. J. McComas (1994b), The heliospheric plasma sheet, *J. Geophys. Res.*, **99**, 6667.
- Zurbuchen, T. H., L. A. Fisk, G. Gloeckler, and R. von Steiger (2002), The solar wind composition throughout the solar cycle: A continuum of dynamic states, *Geophys. Res. Lett.*, **29**(9), 1352, doi:10.1029/2001GL013946.

B. E. Goldstein, P. C. Liewer, and X. Zhou, Jet Propulsion Laboratory, California Institute of Technology, Mail Stop 169-506, 4800 Oak Grove Drive, Pasadena, CA 91109-8099, USA. (bruce.goldstein@jpl.nasa.gov; paulett.liewer@jpl.nasa.gov; xiaoyan.zhou@jpl.nasa.gov)

M. Neugebauer, Lunar and Planetary Laboratory, University of Arizona, Building 92, 1629 E. University Blvd., Tucson, AZ 85721, USA. (mneugeb@lpl.arizona.edu)

J. T. Steinberg, Space and Atmospheric Sciences (NIS-1), Los Alamos National Laboratory, P.O. Box 1663, MS D466, Los Alamos, NM 87545, USA. (jsteinberg@lanl.gov)